Appl Phys B (2012) 106:769–774
DOI 10.1007/s00340-011-4844-1

Applied Physics B
Lasers and Optics

In situ optical measurements of bacterial endospore breakdown in a shock tube

A.D. McCartt · S. Gates · P. Lappas · J.B. Jeffries · R.K. Hanson

Received: 5 June 2011 / Revised version: 20 October 2011 / Published online: 14 January 2012

Abstract The interaction of endospore-laden bioaerosols and shock waves is monitored with a combination of laser absorption and scattering. Tests are performed in the Stanford aerosol shock tube for post-shock temperatures ranging from 400–1100 K. In situ laser measurements at 266 and 665 nm provide a real-time monitor of endospore morphology. Scatter of visible light measures the integrity of endospore structure, while absorption of UV light provides a monitor of biochemicals released by endospore rupture. For post-shock temperatures greater than 750 K endospore morphological breakdown is observed. A simple theoretical model is employed to quantify the optical measurements, and mechanisms leading to the observed data are discussed.

1 Introduction

1.1 Interaction of shock waves and endospores

During periods of environmental stress vegetative bacteria form differentiated cells called endospores. These robust proteinaceous structures are metabolically dormant and highly resistant to harsh environmental conditions. Endospores can survive extreme pressures, elevated temperatures, nutrient depletion, and chemical exposure [1, 2]. This paper presents an experimental protocol for quantifying endospore breakdown in shock-heated gases, analogous to conditions found behind blast waves.

A.D. McCartt (✉) · S. Gates · P. Lappas · J.B. Jeffries · R.K. Hanson
High Temperature Gas dynamics Laboratory, Department of Mechanical Engineering, Stanford University, Stanford, CA 94305, USA
e-mail: mccartt@stanford.edu
Fax: +1-650-7231748

Previous research involving endospore resistance to aerodynamic shock waves has focused on endospores in aqueous suspension [3]. These experiments evaluated the effect of large pressure jumps with negligible temperature rise. Recent experiments studied the interaction of bioaerosols and aerodynamic shock waves in a novel gas dynamic impactor [4]. Bioaerosol flow from a supersonic nozzle is stagnated, causing the biological particulate to pass through a standing normal shock wave. The bioaerosol experiences a large deceleration force, moderate pressure jump, and slight temperature change. While these previous studies examined critical shock-induced pressure and acceleration conditions, this study explores critical shock-induced temperature conditions.

Here we report optical diagnostics for time-resolved monitoring of the interaction of shock waves of controlled strength with aerosols containing bacterial endospores in a shock tube. These experiments used a new laboratory technique, based on the Stanford Aerosol Shock Tube (SAST) [5]. An aqueous suspension of *Bacillus atrophaeusus* (BA) endospores is nebulized into an aerosol, loaded into the SAST, and then shock-heated. The incident and reflected shock waves abruptly heat, compress, and accelerate the bioaerosol. For sufficiently strong shocks, viability reduction and morphology destruction are observed. In this study shock-heated endospores are monitored with time-resolved laser extinction measurements at two wavelengths, 665 nm and 266 nm. The visible light at 665 nm is scattered by bioaerosol particulate. UV light at 266 nm is scattered by particulate and absorbed by UV-active endospore biochemicals released on spore destruction. Thus, the time variation of the transmitted 665 nm intensity provides a time history for the destruction of the endospore morphology, while the transmitted UV light intensity at 266 nm can be used to interpret the release of endospore biochemicals.

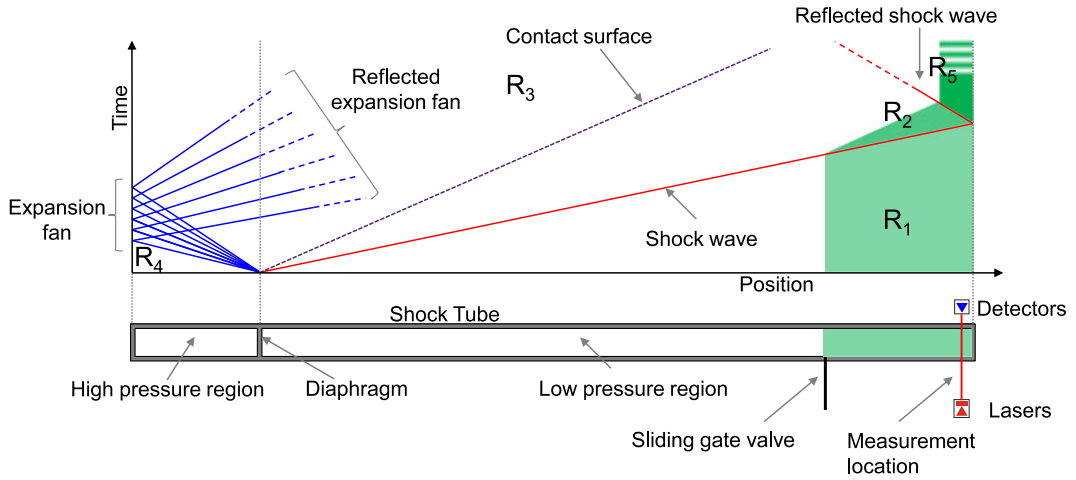

Fig. 1 x–t diagram of the Stanford Aerosol Shock Tube loaded with a bioaerosol (shown in *green*). Region 1 (R_1) represents initial conditions before the arrival of the incident shock wave. Region 2 (R_2) occurs after the passage of the incident shock wave but before the arrival of the reflected shock wave. The steady-state test conditions after the passage of the reflected shock wave are assigned region 5 (R_5)

2 Experimental setup and procedure

2.1 Stanford aerosol shock tube

The Stanford aerosol shock tube (SAST) provides an experimental facility to observe the interaction of bioaerosols and shock waves of controlled strength. A detailed description of bioaerosol loading, shock heating, and sampling procedure can be found in Gates et al. [5]; however, a brief summary is presented below for the reader's benefit. A suspension containing BA endospores and 1 μm SiO_2 beads is nebulized and loaded into the SAST in a carrier gas of pure Argon. The SiO_2 beads are later used for calibration of the viability analysis. The bioaerosol is prevented from diffusing upstream in the tube by a sliding gate valve. The pressure is equalized across the gate valve using pure Argon. Immediately before the test the sliding gate valve is opened, and the high-pressure region is filled with helium until diaphragm ruptures. The gas from the high-pressure region expands behind the ruptured diaphragm, causing the development of a planar shock that propagates down the shock tube. This incident shock wave heats, compresses, and accelerates the test gas. The acceleration of the liquid aerosol breaks large droplets into smaller ones, and the hot gas evaporates the solvent from the endospore-laden aerosol. The shock wave then reflects off the endwall of the shock tube and then reheats, further compresses, and stagnates the endospore-laden mixture. The bioaerosol remains in this steady-state condition for the remainder of the test time (∼2–3 ms). A sample of spore-laden gas is collected from the SAST before and after shock heating for ex situ analysis with flow cytometry, scanning electron microscopy and plating measurements to determine spore viability.

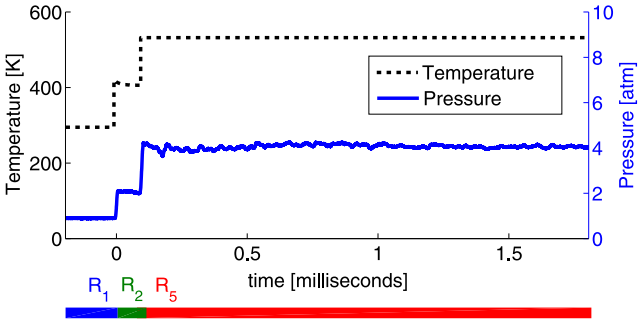

Fig. 2 Calculated temperature and measured pressure conditions at the laser measurement location for a moderate strength shock with $T_5 = 532$. Shock tube regions (R_1, R_2, and R_5) are separated by discrete jumps in temperature and pressure across the incident and reflected shocks

The x–t diagram presented in Fig. 1 details the gas dynamic time history of the SAST for a typical experiment. The horizontal axis represents position along the SAST while the vertical axis represents time beginning with diaphragm rupture. For a given position in the test section, conditions delineated by the passage of shock waves are assigned "regions" for clarity. Region 1 (R_1) represents initial conditions before the arrival of the incident shock wave. Region 2 (R_2) occurs after the passage of the incident shock wave but before the arrival of the reflected shock wave. Finally, the steady-state test conditions after the passage of the reflected shock wave are assigned region 5 (R_5).

Figure 2 shows typical temperature and pressure conditions at the measurement location indicated in Fig. 1. The solid line represents an actual pressure trace from a shock, while the dotted line represents the calculated temperature history. Temperatures behind the reflected shock are highly uniform and vary isentropically with pressure [6]. Isentropic

temperature variations calculated from pressure traces indicate temperature uniformity within 1.5 percent. These temperatures and pressures can be adjusted by manipulating the initial gas pressures.

2.2 In situ diagnostics experimental setup

A combination of laser absorption and laser scattering diagnostics were used for three different in situ monitors of the shock-heated bioaerosol, as illustrated in Fig. 3. Visible light near 665 nm is produced by a single mode Hitachi HL6501MG laser diode, and BBO second-harmonic generation produces UV laser light at 266 nm from a Coherent Verdi Nd:YVO4 5 watt source. The continuous wave laser beams from the UV and visible lasers are combined onto a common optical path, directed across the SAST 2 cm from the endwall, and collected and dispersed in wavelength onto separate detectors. A double-pass optical setup is used to increase the signal-to-noise ratio (SNR) for both the visible and UV diagnostics. Two multiplexed, near-infrared (NIR), fiber-coupled lasers are single-passed through the SAST 5 cm from the endwall to determine time-resolved gas temperature using water vapor absorption.

2.3 Wavelength-multiplexed NIR laser absorption temperature measurements

For pure gas dynamic shock-heating, shock-speed measurements provide accurate values of T_2 and T_5. However, the evaporation of liquid aerosol during region 2 cools the gas and complicates traditional shock-speed-based calculations of temperature. Laser absorption diagnostics can provide an excellent method of temperature measurement in shock tubes [7]. In the present case, water vapor is monitored in the SAST by the ratio of absorption measured using two telecommunications-grade, fiber-coupled diode lasers tuned to transitions with different lower-state energies. Water vapor transitions are chosen in the NIR, near 1343.3 and 1391.7 nm, with lower-state energy values of 1790 and 1045 cm^{-1}, respectively. Each of the lasers is scanned in wavelength over the absorption feature. Rapid scanning of the laser wavelengths provides integrated absorption line strengths for each transition with 50 μs time resolution. Although pressure broadening can complicate the use of this diagnostic for direct temperature measurements in region 5 for some shocks, water absorption measurements from region 2 and the measured shock speed can be used to iteratively solve for the temperature and gas composition in all three regions (1, 2 and 5) [8].

3 Theory

3.1 Beer's law endospore extinction model

A simple model was developed to quantify the UV and visible laser extinction (scatter and absorption). Assuming that at a given axial location and post-evaporation shock region (i.e. 2 or 5) of the SAST, the test gas contains number densities of SiO_2 beads (n_{SiO_2}), intact endospores ($n_{\text{Intact Spores}}$), and destroyed endospores ($n_{\text{Destroyed Spores}}$), and that these have extinction cross sections (σ_i) at 266 nm and 665 nm, the following equations can be formed to represent the transmission at each wavelength:

$$\left(\frac{I}{I_0}\right)_{665\text{ nm}} = e^{-\alpha_{665\text{ nm}}} = e^{-L(n_{SiO_2}\cdot\sigma_{SiO_2}+n_{\text{Intact Spores}}\cdot\sigma_{\text{Intact Spores}})_{665\text{ nm}}} \tag{1}$$

$$\left(\frac{I}{I_0}\right)_{266\text{ nm}} = e^{-\alpha_{266\text{ nm}}} = e^{-L(n_{SiO_2}\cdot\sigma_{SiO_2}+n_{\text{Intact Spores}}\cdot\sigma_{\text{Intact Spores}}+n_{\text{Destroyed Spores}}\cdot\sigma_{\text{Aromatics}})_{266\text{ nm}}} \tag{2}$$

Visible extinction ($\alpha_{665\text{ nm}}$) is attributed completely to scatter from bioaerosol particulate: endospore morphology ($\sigma_{\text{Intact Spores}}$) and SiO_2 beads (σ_{SiO_2}). The model designates two states for endospores, wholly intact or completely destroyed. Destroyed endospores are viewed as disintegrated and hence do not scatter light. In support of this model, high-temperature measurements have shown no evidence of 665 nm absorption resonance with the compounds comprising endospores or the products of endospore pyrolysis. Therefore, it is assumed that destroyed endospores ($n_{\text{Destroyed Spores}}$) have no visible cross-section coefficient. Finally, SiO_2 beads and their cross sections are not affected by the shock conditions. Thus, the post-shock visible extinction provides a time history for the destruction of the endospore morphology.

UV extinction ($\alpha_{266\text{ nm}}$) results from a combination of bioaerosol particulate scatter and UV-active endospore biochemical absorption. While the endospores remain intact, absorption from UV-active biochemicals within the endospore and scatter from endospore morphology contribute to the 266 nm intact endospore coefficient of extinction ($\sigma_{\text{Intact Spores}}$) [9–11]. For high-temperature shocks,

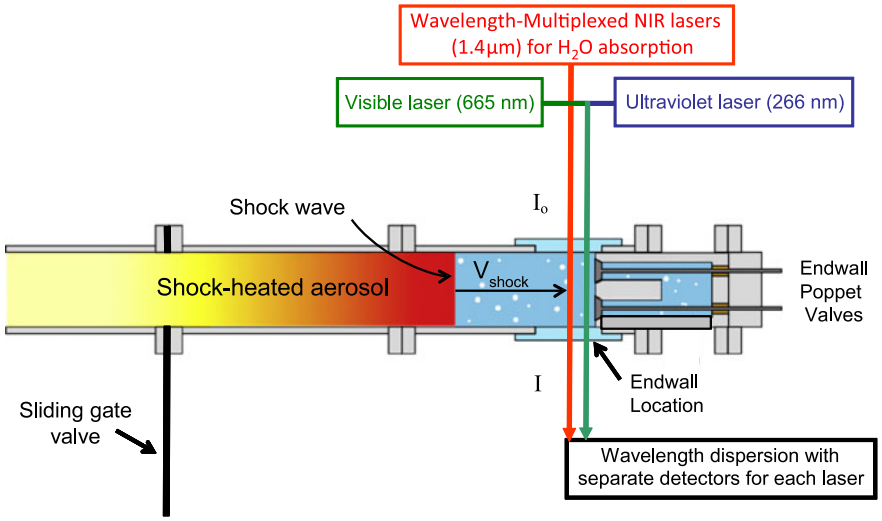

Fig. 3 Schematic of in situ diagnostics experimental setup

endospore morphology will completely break down. As the endospores break up behind the reflected shock, UV-active aromatic biochemicals, such as DPA, nucleic acids, and proteins, are released into the surrounding gas. Prior research has shown that these biochemicals will quickly pyrolyze into stable aromatic products [12]. The aggregate absorption of all UV-active aromatic products from one destroyed endospore is represented by a single, per-destroyed-endospore cross section ($\sigma_{\text{Aromatics}}$). Elevated levels of UV extinction resulting from these UV-active aromatic products provide a monitor for endospore rupture.

The highest temperature shocks, where complete endospore disintegration occurs, were used to determine the endospore extinction coefficients. The sustained visible scatter, after disintegration, arose solely from the SiO_2 beads. Using the known visible Mie scattering coefficient, the number density of SiO_2 beads (n_{SiO_2}) was determined. This measurement in combination with the known endospore-to-bead ratio was used to determine the remaining unknown extinction coefficients. Endospore morphology and biochemical content depended on growth procedure. Although a strict growth procedure was followed to minimize differences in the BA endospore extinction coefficients for different experimental campaigns, some variations were unavoidable. To mitigate these variations, endospore suspensions were homogenized, and extinction coefficients were recalibrated for each experimental campaign.

4 Results and discussion

4.1 Low-temperature shocks

For low post-shock temperatures (T_5), where the endospores remain intact, both extinction signals undergo step changes

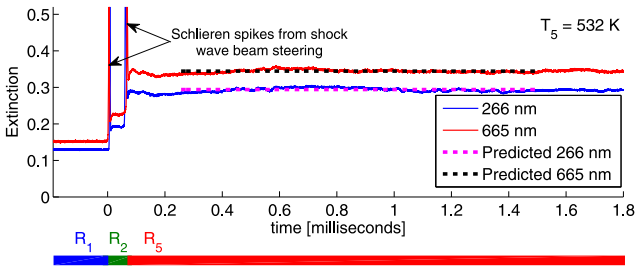

Fig. 4 Extinction (α_i) plotted versus time for in situ diagnostics at 266 nm (*blue*) and 665 nm (*red*) for low-temperature shock ($T_5 = 532$ K). No decay is seen in region 5. Step changes in extinction correspond to density jumps across shock waves. Predicted extinction values (*dotted lines*) are calculated with shock-jump equations and region 2 extinction values

in density as the shock waves pass through the optical beam path. Extinction (α_i) is plotted versus time in Fig. 4 for a low post-shock temperature ($T_5 = 532$ K).

Step changes in extinction correspond to discrete jumps in density across the incident and reflected shock waves. Using the shock-jump relations and region 2 extinction values, the extinction in region 5 can be predicted [13]. The predicted extinctions are represented by dotted lines in Fig. 4. For this temperature, measured and predicted values agree, and extinction remains relatively constant during region 5. This indicates minimal endospore morphology breakdown for this low-temperature condition.

4.2 High-temperature shocks

For cases with high post-shock temperatures (T_5), the visible scatter from the shock-heated spores showed evidence of endospore morphology destruction, while absorption from UV-active biochemicals at 266 nm indicated endospore rup-

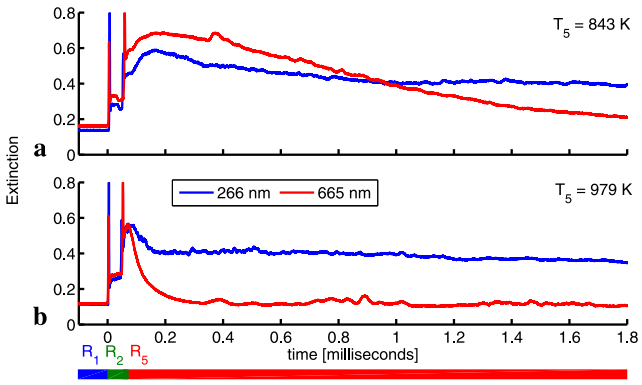

Fig. 5 Extinction (α_i) plotted versus time for in situ diagnostics at 266 nm (*blue*) and 665 nm (*red*) for high-temperature shocks. Endospore breakdown is observed by decreasing region 5 visible scatter. Breakdown rates increase with temperature. Relatively elevated levels of UV extinction result from absorption by pyrolyzed UV-active endospore biochemicals

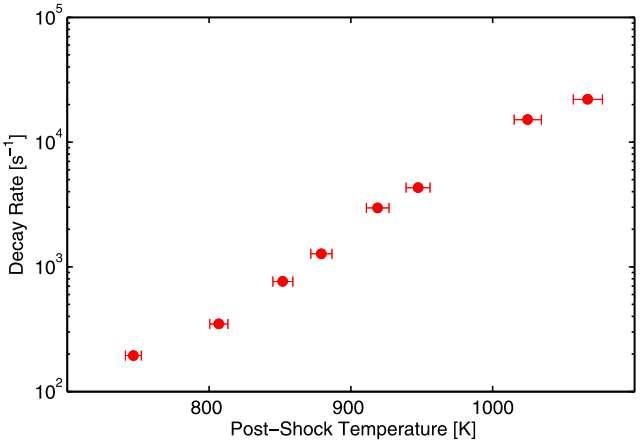

Fig. 6 First-order decay rates of morphology breakdown versus temperature (T_5) are plotted from decay in the 665 nm extinction resulting from intact endospores

ture. Extinction data for two high-temperature shocks are plotted in Fig. 5.

Comparing the 843 K post-shock temperature data in panel (a) to the 532 K data in Fig. 4, the visible extinction has a noticeable decrease with time during region 5. This decrease in extinction is a real-time measurement of endospore morphology breakdown. For higher post-shock temperatures (T_5) morphology breakdown rates increase and eventually complete endospore disintegration will occur within the region 5 test time (as is seen in panel (b)). For shocks with slower but significant breakdown rates, an initial short-term rise in extinction was observed for both wavelengths (as is seen in panel (a)). The initial breakup of intact endospores is hypothesized to decrease the individual volume of endospore particulate but briefly increase the total scattering cross section. Morphological breakdown correlation to elevated pressures and endospore destruction across shock waves were not observed, suggesting that mechanical stresses due to the shock waves and elevated pressures during the test time have limited effects on the shock-induced breakdown of endospores.

The time-dependent UV extinction differed from the visible extinction due to absorption by UV-active biochemicals released as the endospores breakdown. The UV extinction signal includes absorption from gas phase biochemicals and UV scattering from the endospores and the SiO_2 beads (analogous to the scattering experienced by the non-absorbing visible beam). For high-temperature shocks where the endospores were completely destroyed (e.g., Fig. 5b), the UV extinction asymptotes to an elevated constant value due to the biochemical adsorption and scattering from SiO_2 beads, whereas the visible extinction at long times is due only to scattering from the SiO_2 beads. At lower temperatures, see Fig. 5a, a short-term rise in extinction was observed similar to that seen for the visible extinction time histories. However, the subsequent decline in UV extinction is slower and the long-time extinction levels are elevated due to the additional UV absorption from the biochemicals that are released as the endospores breakdown.

4.3 Analysis and discussion

Experiments were performed over a range of post-shock temperatures (T_5) and the data were quantified using (1) and (2) above. Using the visible laser time history and (1) above, the rate of endospore breakdown at different temperatures was assessed. After being thermally excited, both the pyrolysis of molecules in a shock tube and the heat-induced denaturation of proteins in solution have been modeled by first-order kinetics [14–17]. While the models do not readily apply to endospore breakdown in a shock tube, it is instructive to frame our results within a common paradigm. After the initial thermal loading and breakup of endospores (i.e. after the short-term rise in extinction), decay in visible extinction is used to calculate the first-order rates of endospore breakdown. The linear trend seen in Fig. 6 indicates a clear exponential temperature dependence of the first-order endospore breakdown rates.

The amount of damage to endospore morphology that occurs during the region 5 test times can be determined by two methods. The number of endospores that remain intact can be directly calculated from 665 nm endospore scatter ($n_{\text{Intact Spores}}$ in (1)). Alternatively, the number of endospores that have ruptured can be measured from 266 nm extinction due to absorption from biochemical aromatic products ($n_{\text{Destroyed Spores}}$ in (2)). The $n_{\text{Intact Spores}}$ and $n_{\text{Destroyed Spores}}$ values are calculated after the region 5 decay and are plotted in Fig. 7 as the fraction of their predicted values.

The 665 nm scatter from endospore morphology directly measures the percentage of endospores that remain intact.

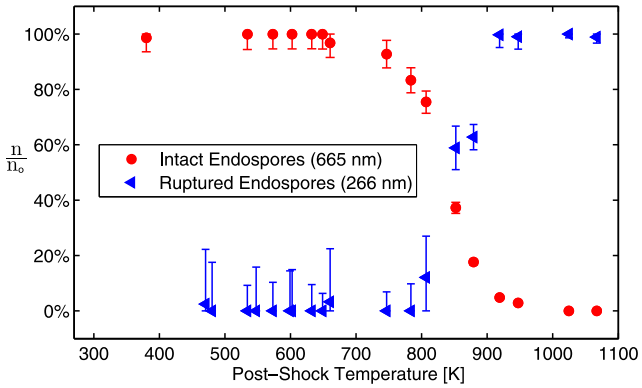

Fig. 7 Percentage of endospores that remain intact (*circles*) or have ruptured (*triangles*) after the region 5 test time are plotted versus post-shock temperature (T_5). The intact and ruptured percentages measurements are derived from 665 nm and 266 nm data, respectively

The 665 nm data indicate that significant endospore damage only occurs for post-shock temperatures above 750 K. However, for post-shock temperatures (T_5) of 600 K where visible scatter indicates no apparent endospore damage, ex situ analysis finds only 0.1% of endospores remain viable [5]. Measured reduction in viability observed before endospore morphological breakdown provides evidence of a mechanism for viability loss that precludes endospore disintegration. We speculate that disruptions to internal biochemical pathways essential to germination or vegetative cell metabolic activity are responsible for the observed viability loss. The ruptured endospore percentage in Fig. 7 above is calculated from the absorption of 266 nm light by released endospore biochemicals. For temperatures below 750 K where endospores have not broken-down, the extinction at 266 nm is due to SiO_2 beads and intact endospores. The attempt to measure near-zero pyrolyzed endospore biochemical signal results in large error bars at low temperatures. However, for test above 850 K with significant biochemical release, the 266 nm data corroborate the 665 nm data.

5 Conclusion

The SAST combined with novel in situ measurement techniques allows for the observation of endospore response to a range of shock wave conditions. BA endospore morphology is shown to break down in shock-heated flows above 750 K with complete endospore disintegration occurring within the 2–3 ms test time for shocks above 950 K. The data obtained from the in situ measurements taken in conjunction with ex situ analysis of post-shock endospore viability provide evidence of an internal deactivation mechanism(s) that precedes endospore disintegration. In the future, tests on mutant endospore strains could be used to elucidate which specific proteins and structures confer resistance to shock wave induced morphological destruction.

Acknowledgements This work was supported by the Defense Threat Reduction Agency via grant AB07TAS014, administered by the Army Research Office under grant 51532CHCBB with Dr. Jennifer Becker of the Chemical Sciences Division as contract monitor.

References

1. P. Setlow, Microbiology **101**, 514 (2006)
2. W.L. Nicholson, N. Munakata, G. Horneck, H.J. Melosh, P. Setlow, Microbiol. Mol. Biol. Rev. **64**, 548 (2000)
3. H. Lundbeck, O. Sköldberg, Biotechnol. Bioeng. **5**, 167 (1963)
4. P.R. Sislian, J. Rau, X. Zhang, D. Pham, M. Li, L. Mädler, P.D. Christofides, Chem. Eng. Sci. **65**, 4803 (2010)
5. S.D. Gates, A. McCartt, P. Lappas, J.B. Jeffries, R.K. Hanson, L.A. Hokama, K.E. Mortelmans, Microbiology **109**, 1591 (2010)
6. A. Farooq, J.B. Jeffries, R.K. Hanson, Appl. Phys. B **96**, 161 (2009)
7. R.K. Hanson, Proc. Combust. Inst. **33**, 1 (2011)
8. D.F. Davidson, D.R. Haylett, R.K. Hanson, Combust. Flame **155**, 108 (2008)
9. S.H. Pendukar, P.R. Kulkarni, Food/Nahrung **32**, 1003 (1988)
10. C.G. Mallidis, J.S. Scholefield, J. Appl. Bacteriol. **59**, 479 (1985)
11. P.S. Tuminello, E.T. Arakawa, B.N. Khare, J.M. Wrobel, M.R. Querry, M.E. Milham, Appl. Opt. **36**, 2818 (1997)
12. R. Goodacre, B. Shann, R.J. Gilbert, É.M. Timmins, A.C. McGovern, B.K. Alsberg, D.B. Kell, N.A. Logan, Anal. Chem. **72**, 119 (1999)
13. J.B. Young, A. Guha, J. Fluid Mech. **228**, 243 (1991)
14. P.L. Privalov, N.N. Khechinashvili, J. Mol. Biol. **86**, 665 (1974)
15. M. Röhrig, E.L. Petersen, D.F. Davidson, R.K. Hanson, Int. J. Chem. Kinet. **29**, 483 (1997)
16. E.I. Shakhnovich, A.V. Finkelstein, Biopolymers **28**, 1667 (1989)
17. M. Weijers, P.A. Barneveld, M.A. Cohen Stuart, R.W. Visschers, Protein Sci. **12**, 2693 (2003)